Indonesian Geotechnical Journal, August Year 2023, Vol 2 (2). Page 21 - 38
DOI: https://doi.org/10.56144/igj.v2i2.43
EISSN: 2829-7520
https://indonesian-geotechnical-journal.org/index.php/JGI/issue/archive

Identification of Vulnerability Due to the Pasaman M6.2 Earthquake on 25 February 2022 Using Satellite-Based Methods and Field Surveys

Edy Santoso[1*], Sigit Pramono[1], Dadang Permana[1], Muzli Muzli[1], Bambang Setyo Prayitno[1], Dwikorita Karnawati[1]
[1]Indonesian Agency for Meteorological, Climatological and Geophysics, Jakarta, Indonesia, 10720
*Correspondence: edy.santoso@bmkg.go.id

SUBMITTED 26 April 2023 **REVISED** 8 June 2023 **ACCEPTED** 19 June 2023

ABSTRACT The Pasaman earthquake which occurred on 25 February 2022, with a magnitude of 6.2, caused casualties and infrastructure damage. Vulnerability identification determines the potential extent to which a system or unit tends to be damaged. Vulnerability identification in this study was carried out based on four vulnerability indicators, namely: rate of soil movement from satellite image processing, soil type classification based on Vs30, corrected isoseismal shakemap, and residential area maps. Each indicator, with their respective weightage, is then scored and summed to evaluate the vulnerability of areas in the vicinity of Pasaman earthquake. The processing of Sentinel-1 SLC satellite data using the advanced Differential Interferometric Synthetic Aperture Radar (DInSAR) produces a deformation rate around area of epicenter. Areas that have high vulnerability generally have a value of ground movement rate in the form of subsidence above 5 cm/year. These areas were predominantly residential and experienced significant damage during the earthquake. The soil type in these regions was classified as medium soil, and the intensity of shocks during the earthquake was categorized as VI MMI or higher. This study was conducted in the area near the epicenter of the Pasaman earthquake, such as in the district Pasaman, Bonjol, Pasaman, Palembaya, and Lubuk Basung. A study of disaster vulnerability identification is carried out to reduce the losses and minimizing the exposure of the population to disasters. The results of vulnerability identification can be used as part of education and literacy to reduce the risk of earthquake disasters.

KEYWORDS The Pasaman earthquake; Vulnerability; Subsidence

1 INTRODUCTION

Earthquake are considered one of the most destructive natural disasters. An earthquake is a natural event in the form of vibration or wave motion on the earth's surface caused by a sudden release of energy from below the earth's surface. The energy that causes earthquakes is released through active faults. Earthquakes usually cause changes in the shape or position of the earth's surface (deformation). Based on the time of occurrence, deformation can be grouped into three, namely deformation after (post-seismic), during (co-seismic), and before (inter-seismic) earthquake (Panuntun et al. 2018).

Earthquake mitigation before and after the incident is the key to minimizing casualties. Maps are an important instrument to support the post-event mitigation process (Markogiannaki et al. 2020). The map is used to identify vulnerabilities after an earthquake so that potential damage can be identified in the event of a similar earthquake. As the area affected by earthquake is wide, many data points are required to identify the vulnerabilities. Unfortunately, position information generated from observations of seismic equipment is limited to a single observation point of the equipment. To obtain more data points, observations with microwave-based remote sensing techniques is one of the possible alternatives. By utilizing active microwave images produced by synthetic radar satellites (Synthetic Aperture Radar Satellite), recording of the earth's surface conditions can also be done even with presence of clouds. Figure 1 illustrates how SAR satellites process the data before and after an earthquake event. In its utilization, Synthetic Aperture Radar (SAR) images are processed using the

Interferometric Synthetic Aperture Radar (InSAR) method. InSAR is one of the remote sensing techniques to detect surface deformation caused by earthquakes (Xu et al. 2020). Processing based on SAR Sentinel-1 SLC satellite imagery with one of the InSAR methods, namely Differential SAR (DInSAR), produces deformation in the surrounding area which is represented by the speed of Line of Sight Displacement (LOS Displacement). This processing is carried out using a cloud computing platform, the Geohazard Exploitation Platform (GEP), developed by the European Space Agency (ESA).

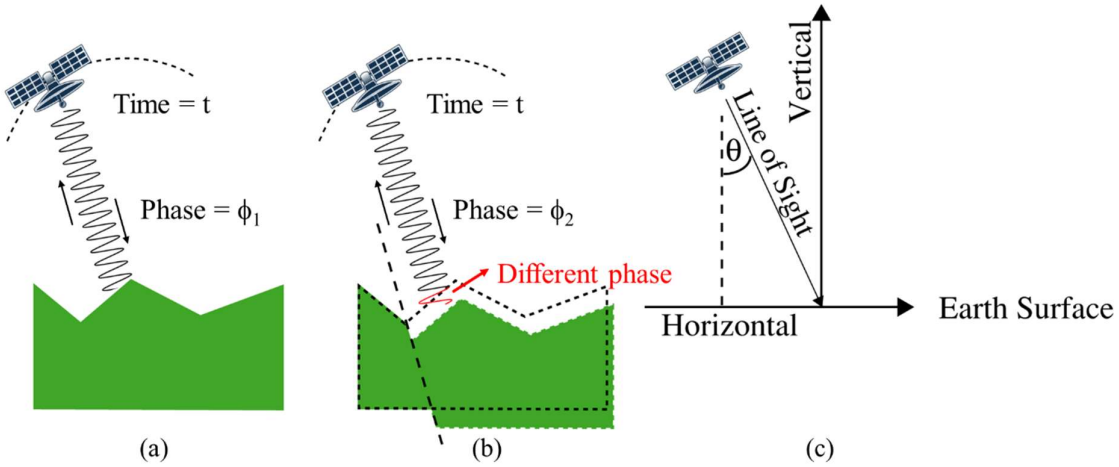

Figure 1. Illustration of SAR image recording during (a) *t* before the earthquake, (b) *t* after the earthquake, and (c) the geometry of the Satellite Line of Sight. The incident angle is θ. The black arrows in (a) and (b) indicate the direction of arrival and return of the satellite sensor signal.

The Pasaman earthquake occurred on Friday, February 25, 2022, at 08:39:00 WIB (Western Indonesian Time) with a magnitude of 6.2. The epicenter is located at coordinates 0.15 °N - 99.98 °E, Northeast of Pasaman, West Sumatra, Indonesia. The earthquake that occurred can be categorized as shallow earthquake (depth 12 km), caused by fault shift activity which had a dextral slip fault movement mechanism. Based on the hypocenter of this earthquake, it is thought to be associated with the Sumatran Fault Zone in the West Pasaman area. The fault is called Sumatran Active Fault Lubuk Sikaping Segment, with ± 65 km long and average shift of 14 mm/year with the characteristics of Terbanan, fault escarpments, facet triangles, fan deposits, terraces, sturdy and fracture. This fault is found in Paleozoic – Cenozoic rocks and rocks of Talamau Volcano, Gunungapai Sarik (Pleistocene-Holocene).

The earthquake has caused shocks in several areas with an intensity between II to VIII on the Mercalli Modified Intensity (MMI) scale. This earthquake has resulted in the death of 27 people, 457 injured and 19221 people were displaced. The Pasaman earthquake also resulted in thousands of buildings to suffer light to heavy damage.

2 GENERAL SOIL AND GEOLOGICAL CONDITIONS

The types of soil that can be found in Lubuk Sikaping, Pasaman Regency (Figure 2) are: Litosol type from alluvial material, igneous rock, volcanic rocks Red-Yellow Podzolic, Latosol and Litosol from metamorphic sedimentary igneous rocks in low fault mountains, and Brown Podzolic of Alluvial material on high fault mountains. Majority of the soil that can be found in Pasaman Regency are Litosol type and Red-Yellow Podzolic type, which cover 27.01% (106,619 Ha) and 26.34% (103,988 Ha) of the total area, respectively.

Soil texture found in Pasaman Regency is generally dominated by fine texture, which is spread in every sub-district. Whereas other texture classifications are minority, generally found in Rao District, Mapat Tunggul District and Panti District.

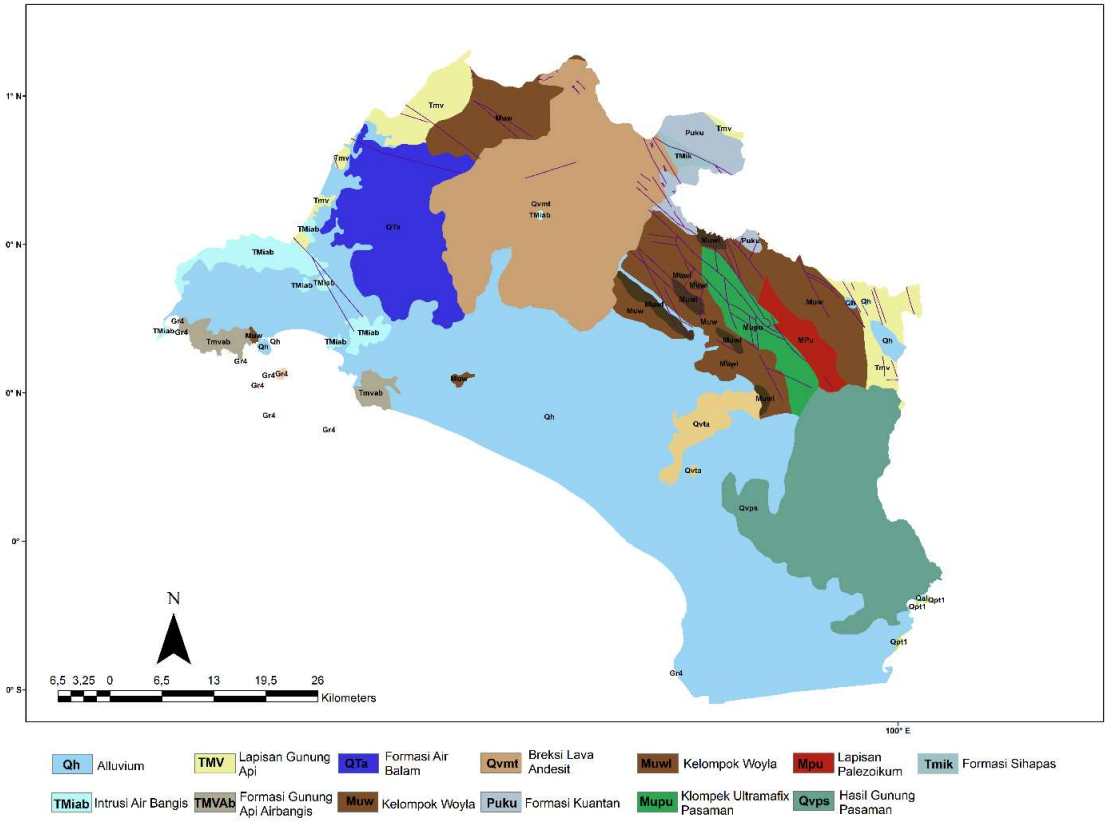

Figure 2. Geological map of Lubuk Sikaping, Pasaman Regency (Rock et.al, 1983)

Morphologically, the closest areas affected by earthquake shocks are plains and hills that are undulating to steep. The area is generally composed of Pre-Tertiary rocks in the form of metamorphic rocks, Tertiary-aged rocks in the form of sedimentary rocks and volcanic debris, and Quaternary deposits. The western part is Quaternary deposits. Steep slopes formed by fault lines will become landslide-prone areas. Quaternary deposits and rocks of Pre-Tertiary and Tertiary age that have undergone weathering are soft, loose, unconsolidated, and strengthen the effects of shocks, making them prone to earthquakes. In addition, the morphology of the hills which are composed of Pre-Tertiary and Tertiary rocks that have undergone weathering has the potential for soil movement to occur.

3 DATA ACQUISITION AND METHODOLOGY

3.1 Data

The area of this study is limited to latitude -1,670 LS - 0.209 LU and longitude 98,00779 E - 100,311 E. The reference center point uses the Minangkabau Padang airport runway point 0.7867 LS -100.2806 E. Due to the expected magnitude of ground displacements and the abundance of data available over the area of interest, we restricted our analysis to Sentinel 1A data only with rate of sampling = 12 days (Table 1). Sentinel satellite - 1A is a type of radar satellite owned by the European Space Agency which is used for deformation observations on the earth's surface with a wavelength of 5.66 cm (C - Band). In total, there are 15 data acquisitions from October 3, 2021 to March 20 2022. The time period of data collection is considered to represent the conditions before (inter-seismic), shortly after (co-seismic), and after the (post-seismic) occurrence. Deformation due to earthquakes is the data recorded. The data is available on the GEP platform, containing phase and intensity information covering an area of up to 250 km^2 in an interferometric wide (IW) swath mode with spatial

resolutions ranging from 5 to 20 meters and with polarization mode vertical-vertical (VV) and vertical-horizontal (VH). Processing of the data uses DEM SRTM-1 and the chosen coherence level is 0.85.

Table 1. Sentinel-1 SLC Satellite data were used for processing, along with the first and last images of each dataset, the product type, polarization mode, and band.

No	Acquisition date	Product Type	Polarization Mode	Band
1	2022-03-20	Sentinel-1 SLC	VV+VH	C
2	2022-03-08	Sentinel-1 SLC	VV+VH	C
3	2022-02-24	Sentinel-1 SLC	VV+VH	C
4	2022-02-12	Sentinel-1 SLC	VV+VH	C
5	2022-01-31	Sentinel-1 SLC	VV+VH	C
6	2022-01-19	Sentinel-1 SLC	VV+VH	C
7	2022-01-07	Sentinel-1 SLC	VV+VH	C
8	2021-12-26	Sentinel-1 SLC	VV+VH	C
9	2021-12-14	Sentinel-1 SLC	VV+VH	C
10	2021-12-02	Sentinel-1 SLC	VV+VH	C
11	2021-11-20	Sentinel-1 SLC	VV+VH	C
12	2021-11-08	Sentinel-1 SLC	VV+VH	C
13	2021-10-27	Sentinel-1 SLC	VV+VH	C
14	2021-10-15	Sentinel-1 SLC	VV+VH	C
15	2021-10-03	Sentinel-1 SLC	VV+VH	C

The BMKG survey team conducted a shallow refraction seismic survey using the multichannel analysis of surface waves (MASW) method. The MASW is used to obtain averaged shear wave velocity for the upper 30 m of soil from the ground surface. This averaged shear wave velocity is called Vs30. The survey was conducted around the area damaged with a radius of about 12 km by the epicenter. The total number of measurement points around the affected location area is 7 points. Due to the limited human resources, time and costs as well as difficulty in accessing some locations for measurement, only 7 MASW measurement points were carried out. The data was considered to represent the conditions of the damaged site. The results of MASW are tabulated in table 2. The Vs30 values obtained ranged from 226.79 - 330.73 m/s. According to SNI 1726; 2019 soil type classification table, the soil in all measurement points is classified as medium soil type (SD). The MASW survey measurement data were added to the USGS Vs30 model data.

Table 2. Locations and measurement results of field MASW survey

No	Long.	Lat.	Description	Vs30 (m/s)	Site Class
1	99.978	0.221	Baiturahim Mosque	226.79	SD (medium Soil)
2	99.930	0.166	Kajai Roboh Mosque	330.15	SD (medium Soil)
3	99.972	0.180	Simpang Nagari Administrative Area	312.82	SD (medium Soil)
4	99.827	0.109	Pasaman Barat Regent Office	317.82	SD (medium Soil)
5	99.939	0.150	Crack Location	330.73	SD (medium Soil)
6	99.946	0.172	MAN 4 Islamic School	258.99	SD (medium Soil)
7	100.049	0.046	Tigo Nagari subdistrict, Malampa	241.50	SD (medium Soil)

Figure 3 shows a composite shakemap around the epicenter of Pasaman 25 February 2022 earthquake is derived from real data recordings of PGA accelerographs and the model of Worden et al., 2012. Other supporting data used in this study uses data on the distribution of population settlements in 2020.

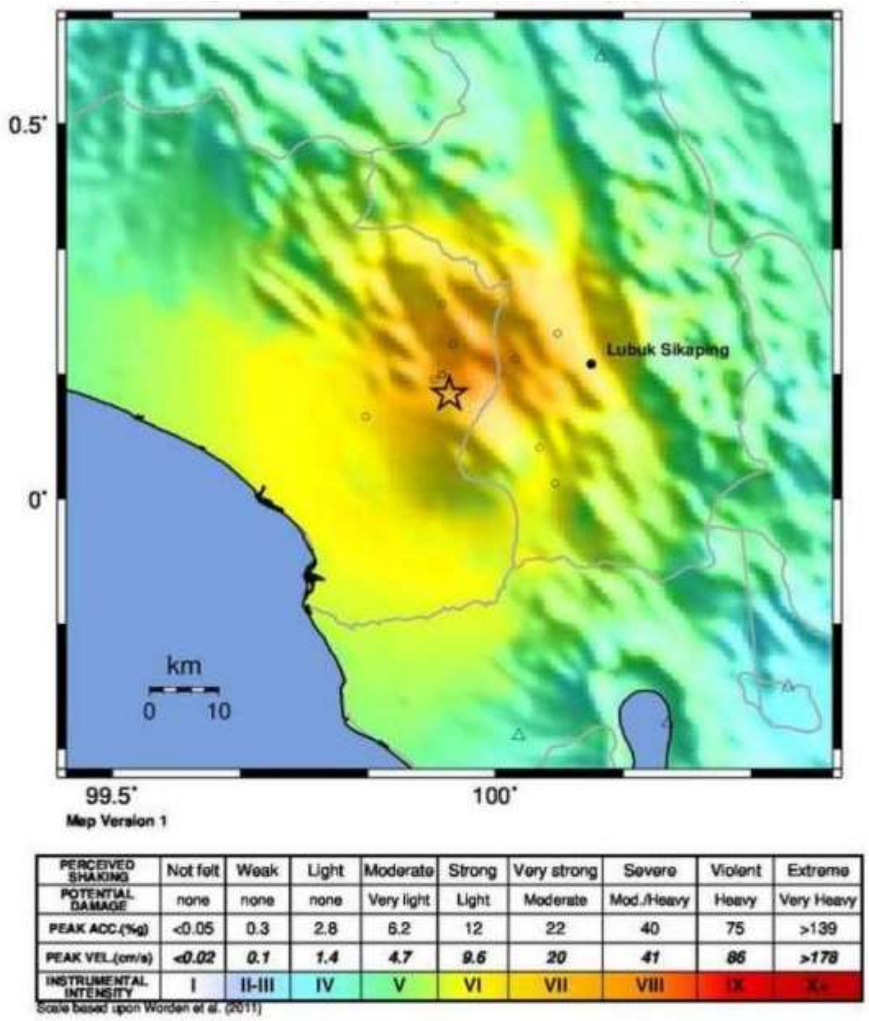

PERCEIVED SHAKING	Not felt	Weak	Light	Moderate	Strong	Very strong	Severe	Violent	Extreme
POTENTIAL DAMAGE	none	none	none	Very light	Light	Moderate	Mod./Heavy	Heavy	Very Heavy
PEAK ACC.(%g)	<0.05	0.3	2.8	6.2	12	22	40	75	>139
PEAK VEL.(cm/s)	*<0.02*	*0.1*	*1.4*	*4.7*	*9.6*	*20*	*41*	*86*	*>178*
INSTRUMENTAL INTENSITY	I	II-III	IV	V	VI	VII	VIII	IX	X+

Scale based upon Worden et al. (2011)

Figure 3. Shakemap corrected (star symbol signifies the epicenter of earthquake)

3.2 Methodology

3.2.1 Satellite Image Processing Method

Sentinel 1A radar satellite imagery is used to determine surface deformation before and after an earthquake. The deformation can be in the form of ground subsidence or ground uplift. License to use and process sentinel 1A satellite data through the geohazard application from Terradue is supported by the Asian Development Bank (ADB). The spatial resolution of the sentinel-1 A radar satellite in the digital elevation model in the satellite imagery data processing methodology is around 12.5 x 12.5 m. The multi temporal spatial analysis (MTA) methodology is capable of imaging post-earthquake conditions by using images captured before and after the Pasaman 25 February 2022 earthquake. Accurate surface deformation maps in the form of subsidence or uplift were obtained using the InSAR (Interferometry synthetic aperture radar) technique. SAR is a form of a ground reflectivity image using active remote sensing. The antenna transmits radiation that is reflected from the image area. The change in signal phase, or interference, over time is the principle of InSAR (Soza, 2018). Using InSAR, large areas can be monitored without the need for field measurements and, therefore, the cost of monitoring is very low. The basic principle of this method is that when a point on the surface moves, a change in the distance between the sensor and the point on the ground also changes. This results in a change in the phase value recorded by SAR sensors moving along the orbit (Gens and Logan 2003).

High spatial resolution image recordings obtained from sensors, called assets, are the definition of SAR. Signal processing uses the magnitude and phase of the received signal on successive pulses to create an image from a synthetic or virtual aperture antenna consisting of sequential and consistent radar signal vectors. Radar signals that are transmitted and received by small antennas that move along a specific orbit (Sillerico et al. 2010; Vidal Montes et al. 2016; Martinez-Graña et al. 2015; Martínez-Graña et al. 2016). Calculation of the time and lag measurements of the distance between the satellites and the surface area produces interferometric data. A direct comparison between the interferometric phases over a range of surface characteristics with any change from two observations at the same location in space but at different times.

When there is ground deformation *D(t)*, the Synthetic Aperture Radar sensor obtains an image at time *t0* for the first time with a measured phase of Φ_M. The first SAR satellite imagery is usually referred to as the master, *M*. If the observed point is *P*, the displacement within a certain period of time is called *P1*. If two images are used, then the second SAR image has time *t* and phase Φ_S. The second and subsequent SAR satellite images are named slave, *S*. The $\Delta\Phi_{Int}$ interferometric phase is a technique for InSAR processing by exploiting the difference in Φ_S and Φ_M phases. The key element for InSAR DEM (Digital Elevation Model) processing is to make an assumption that *D(t)* does not exist. To make *D(t)* non-existent, the assumption is that the field is stable, and thus *P1* assumes that the difference in *SP-MP* distance will coincide with each other. As the point moves from *P* to *P1* between the two image acquisitions, the topographical phase components Φ_{topo} and $\Delta\Phi_{Int}$ include the contribution of the field movement, Φ_{Mov}. In general $\Delta\Phi_{Int}$ can be calculated with:

$$\Delta\Phi_{Int} = \Phi_S - \Phi_M = \frac{SP - SM}{\frac{\lambda}{4.\pi}} + \frac{SP^1 - SP}{\frac{\lambda}{4.\pi}} + \Phi_{Atm} + \Phi_{Noise} = \Phi_{Mov} + \Phi_{Atm} \quad (1)$$

where Φ_{Atm} is the atmospheric contribution; Φ_{Noise} is the phase noise; SP^l is the slave-to-P^l distance; and λ is the radar wavelength. As mentioned above, using the topographic component, Φ_{Topo} is possible to generate a DEM of the observed scene. In the InSAR techniques, the inverse transformation is used: if a DEM of the imaged scene is available, Φ_{Topo} can be simulated and subtracted from $\Delta\Phi_{Int}$, obtaining the so-called InSAR phase $\Delta\Phi_{D-Int}$:

$$\Delta\Phi_{D-Int} = \Delta\Phi_{Int} - \Phi_{Topo\_Sim} = \Phi_{Mov} + \Phi_{Atm} + \Phi_{Res\_Topo} + \Phi_{noise} \quad (2)$$

In order to obtain information about terrain movement, the simulated topographic component, represented by ΦTopo_Sim, must be separated from the residual component, denoted by ΦRes_Topo. This is because of errors in the simulation process when using digital elevation model (DEM). Figure 4a shows the process of separating these components. Two-pass interferometry techniques that employ an external DEM are used to derive the topographic phase component. Alternatively, three-pass interferometry can be used without an a priori known DEM, but at least three images must be acquired over the same scene. Sentinel images in the C band are used to determine deformation and accumulated displacement over a period of October 3, 2021 to March 20, 2022, period before and after the Pasaman February 25 2022 earthquake. Sentinel-1 SLC imagery was processed using the Parallel Small Baseline Subset service developed by CNR-IREA on the GEP platform. In general, the process to produce interferometry images from a pair of SLC format images can be seen in Figure 4a. The explanation of each stage is as follows:

a) Image Co-registration. Co-registration is needed to ensure that the data recorded on the SAR image has the same coordinates. At this stage, the pixels in the slave image are aligned with the pixels in the master image.
b) Formation of the interferogram. This process is carried out after the image correction is complete. At this stage, the master image is cross multiplied with the slave image to form an interferogram.
c) Differential InSAR processing. The steps are taken to reduce noise and reduce topographic effects using DEM data. In this study, the filtering process was carried out using the advanced Goldstein filter method (Goldstein and Werner, 1998).

d) Phase unwrapping. At this stage, the value of the phase difference between the master image and the slave image is converted into a deformation value. The change process is carried out using the SNAPHU algorithm (Chen and Zebker, 2002).
e) Geocoding. This step is carried out to change the coordinate system in the interferogram from a radar coordinate system to a georeferenced coordinate system. The LOS displacement is deformation caused by the earthquake can be calculated using the following equation:

$$\text{LOS } displacement = \frac{\theta.\lambda}{-4\pi} \quad (3)$$

Where is θ the unwrapped phase difference and λ is the wavelength of the Sentinel-1 satellite sensor = 0.056 meters.

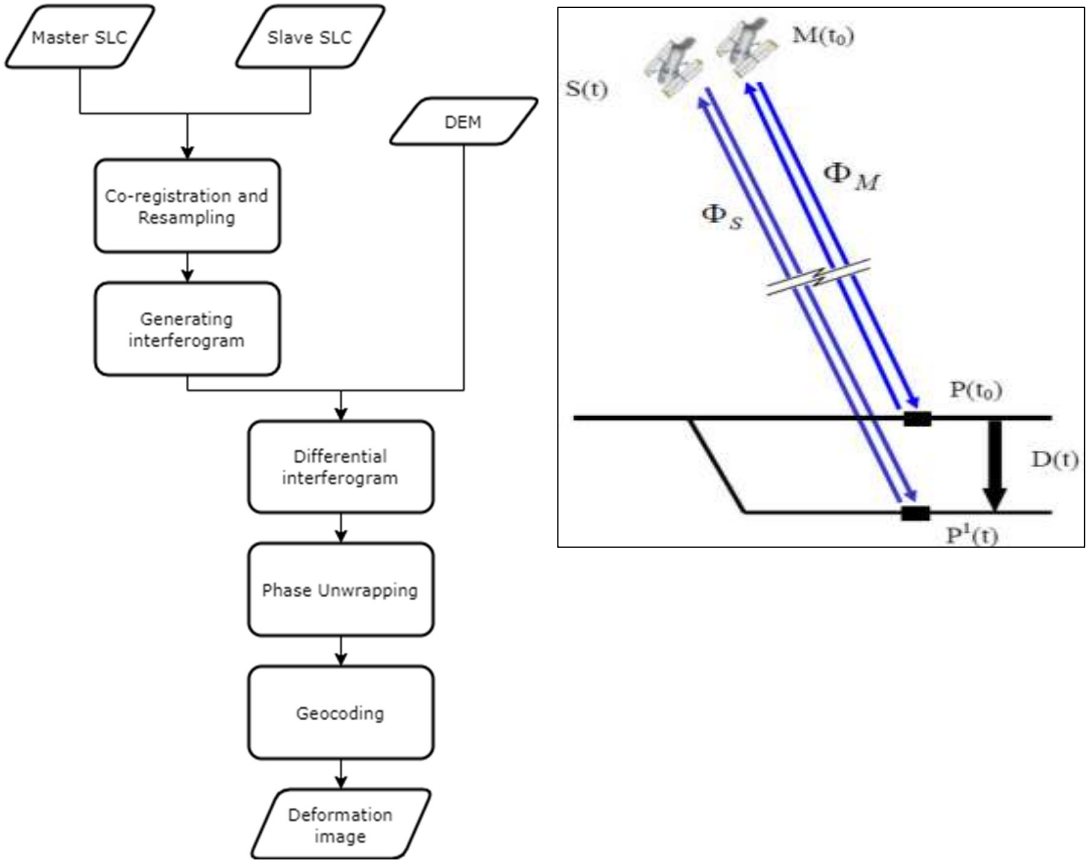

Figure 4. (a) Flowchart of data processing in SLC format with Geohazard-tep. EU, (b) schematic diagram showing relationship between ground displacement and signal phase shift.

3.2.2 Refraction Seismic Survey Data Processing Method

The MASW method is commonly used for site characterization studies and geotechnical investigations because it is non-invasive and provides a rapid and cost-effective means of estimating soil stiffness parameters. The technique involves placing an array of geophones on the ground surface and generating surface waves using a seismic source such as a sledgehammer or a shaker. The surface waves propagate through the soil and are recorded by the geophones. The recorded data is then processed to obtain the dispersion curve, which is a plot of the phase velocity of the surface waves as a function of frequency (Park et al, 2007). To estimate the Vs30 profile from the dispersion curve, a series of mathematical models and inversion techniques are applied. These models and techniques

are based on the principles of wave propagation and soil mechanics, and they use the dispersion curve to infer the shear wave velocity profile of the soil. The Vs30 value is then calculated by averaging the shear wave velocities over the top 30 meters of the soil column. The Vs30 value is an important parameter for seismic hazard assessment and is used in many empirical ground motion prediction equations (GMPEs) to predict ground motion amplitudes during earthquakes. The Vs30 value is also used to classify soils into different categories for building code provisions and seismic design guidelines.

The MASW method has gained significant attention and is now considered a prominent surface wave analysis technique for determining shear wave velocity profiles in civil engineering applications (Xia, 2014). MASW offers advantages such as efficient data acquisition, quicker and less labor-intensive data processing, and improved noise identification and elimination from recorded data (Park et al. 1999; Xia et al. 2000), resulting in more accurate experimental dispersion curves and a more precise shear wave velocity profile. Additionally, the MASW method enables the extraction of higher-mode dispersion curves based on the recorded surface wave data (Xia et al. 2003). This method is a non-invasive geophysical technique used to measure the shear wave velocity profile of the subsurface. The method is based on the principle that Rayleigh surface waves, which are generated by the interaction of shear waves with the surface soil layer, have dispersive properties. This means that the velocity of the Rayleigh surface wave depends on the frequency of the wave, with high-frequency waves propagating to shallow depths at low speeds and low-frequency waves propagating to greater depths at higher velocities. By measuring the velocity of the Rayleigh surface wave at different frequencies, the MASW method can estimate the Vs30 profile, which is a key parameter used to describe the stiffness and strength characteristics of the soil. The MASW method has become one of the key surface wave analysis methods in civil engineering due to its efficient data acquisition routine in the field, faster and less labor-consuming data processing procedures, and improved identification and elimination of noise from recorded data. Additionally, the MASW method can be used to observe and extract higher-mode dispersion curves based on the recorded surface wave data.

The maximum investigation depth in an MASW survey is site-specific and depends on various factors, including the measurement profile's configuration, the natural frequency of the receivers, and the seismic source used (Park and Carnevale 2010; Park et al. 2002, 2007). The longest Rayleigh wave wavelength retrieved determines the investigation depth, and a commonly used empirical criterion (Park and Carnevale, 2010) is adopted to determine the maximum investigation depth:

$$Z_{max} \approx 0.5\ \lambda_{max} \tag{4}$$

The maximum depth of investigation is denoted by Z_{max}, while λ_{max} represents the longest wavelength. The shear wave velocity of the soil up to a depth of 30 meters (Vs30) serves as an indicator of the soil's stiffness and strength properties (Park et al., 2007). The data obtained through the MASW is expressed as a function $r = (i,j)$, where i and j are integer values ranging from 1 to n. To facilitate further analysis, the data is subjected to a long j transformation via Fast Fourier Transform (FFT), as described by Park et al. (1998):

$$R(i,\ k) = \sum_{j=1}^{n} r(i,j)\, e^{\frac{-1\,(j-1)2\pi k}{M}}, note: (k = 1, 2, \ldots . M) \tag{5}$$

The sum above is a discretization of the following equation:

$$U(x,w) = \int u(x,t) e^{twt} dt \tag{6}$$

$$V(w,\emptyset) = \int e^{i\emptyset x} \left[\frac{U(x,w)}{|U(x,w)|}\right] dx \tag{7}$$

Obtaining direct and accurate measurements of the shear wave velocity (Vs) can be challenging and expensive. The MASW is a seismic method that can measure the distribution of shear-wave velocity by analyzing the dispersion of surface waves generated by either an active source or ambient sources. This method uses an array of geophones to measure the seismic waves. To obtain the dispersion curve from the multi-channel recording data, we employed the phase-shift method described by Park et al. (1998). The multi-channel recording data, represented in the time-distance domain, was transformed into the frequency-velocity domain using Fast Fourier Transform (FFT). The Jacobian matrix was then utilized to derive the changes in compression wave velocity, density, and layer thickness as shear wave velocity parameters.

We applied the Contouring Grids technique developed by Xia et al. (2000) to generate a 2-D profile of shear wave velocity by correlating the 1-D profile of each multi-channel data. The Vs30 value represents the average shear wave propagation speed weighted by the thickness of the soil layer, which can be calculated using the following equation:

$$Vs30 = \frac{\sum_{i=1}^{m} ti}{\sum_{i=1}^{m} ti/_{vsi}} \quad (8)$$

where Vs30 is the average shear wave propagation speed at a depth of 30 m in the topsoil layer, *ti* is the thickness of layer i, and *vsi* is the shear wave propagation speed in layer i.

3.2.3 Vulnerability Identification Method

This study focuses on identifying physical vulnerability, which is a component of vulnerability in the form of physical objects that can be lost or damaged when exposed to threats. There are several definitions to Vulnerability. UNISDR Terminology of Disaster Risk Reduction (2009) defines vulnerability as characteristic and situation of a community, system, or asset that makes them susceptible to adverse effects of a hazard or impact. Vulnerability is also a condition of a community or society that leads to or causes an inability to deal with the threat of disaster. PERKA BNPB No. 2 of 2012 assesses vulnerability from a set of conditions and or a result of conditions that adversely affect disaster prevention and management efforts. This component is a physical object that is considered to have value. The indicator is the residential area where the population is located. Residential areas indicate a large population and large economic value of buildings, hence if a disaster were to occur, it can cause a high risk. Vulnerability mapping is carried out to minimize risks from occurrence of disasters. Vulnerability level can be categorized as high, moderate, or low. Using the map, prevention activities can be focused in areas with high level of vulnerability (Arifin, 2010; Herman, 2015). The indicators used to determine the vulnerability level in the area around the epicenter of the earthquake are based on 4 indicators, namely: Los Displacement by satellite image processing indicator, shear wave velocity indicator (Vs30), shakemap corrected indicator and nearby settlement indicators. Line of sight displacement by satellite image processing comes from processing multi temporal analysis method Differential synthetic aperture radar. From this process the deformation rate is obtained in the area around the epicenter of the earthquake. Internal deformation rates range from -5 to 5 cm/yr (negative for subsidence, positive for uplift). The deformation rate are then given score ranging from 0 to 5 (Table 3A). Scoring is given based on potential vulnerability, the higher the value, the higher the level of vulnerability. Subsidence are given a higher scoring value than uplift, while in stable areas with a deformation rate of 0-2.5 cm/s, they are considered not to cause too much vulnerability, so a score of 0 is given. After scoring, the indicator is given a 30% weightage for vulnerability assessment.

The shear wave velocity indicator (Vs30) obtained from the measurement results as well as data from the USGS Vs30 model is given a score ranging from 1 to 5 based on SNI 1726, 2019. The smaller the Vs30 value, the softer the soil type, the higher the risk, hence the higher the score. On the other hand, the greater the Vs30 value, the harder the soil or rock type, the lower the score. The scoring system given in SNI 1726, 2019 is shown in table 3B. Vs30 contributes a weightage of 20% to the vulnerability identification.

The shakemap corrected vulnerability indicator is taken from accelerograph recording equipment, a device for recording earthquake shocks. The corrected shakemap is a map of earthquake shocks in intensity units called the modified Mercalli intensity (MMI). The shock intensity values are classified into 6 classes (from I to VI). The greater the value of the intensity of the shock, the greater the scoring in this classification. From the results of this scoring, each classification is then given a 20% weightage of the level of vulnerability used in the indicator. Table 3C shows the scoring system for shakemap corrected.

The last indicator used is the residential area around the area affected by the Pasaman earthquake. Classification is divided into 2 classes, namely residential areas and non-residential areas, with a score of 5 and 0 respectively. From the results of this scoring, each classification of residential areas is then given a weightage of 30% for the vulnerability assessment. Table 3D shows the scoring system for settlement indicator.

The vulnerability map is the result of summation all vulnerability indicators (equation 9). To determine the level of vulnerability, the total vulnerability score is classified into three classes (low, moderate, and high) using an arithmetic classification by Arifin (2010). The equation is shown in equation 10.

Table 3. Parameters of disaster vulnerability identification

A. LOS Displacement by satellite image processing

Deformation rate of displacement (cm/year)	**Score**	**Weight**
< -5	5	30%
-5 to -2.5	4	
-2.5 to 0	3	
0 to 2.5	0	
2.5 to 5	1	
> 5	2	

B. Shear wave velocity (Vs30)

Vs_{30} (m/s)	**Score**	**Weight**
Vs < 175	5	20%
175 < Vs <350	4	
350 < Vs <750	3	
750 < Vs <1500	2	
Vs > 1500	1	
Vs < 175	5	

C. Shakemap corrected

MMI	**Score**	**Weight**
≥VI	5	20%
V	4	
IV	3	
III	2	
II	1	
≤ I	0	

D. Settlements

Location	**Score**	**Weight**
Settlement	5	30%
Non Settlement	0	

Vulnerability Identification (VI) =

$$(30\% * \text{Deformation}) + (20\ \% * Vs_{30}) + (30\ \% * \text{Settlements}) + (20\ \% * \text{Shakemap}) \quad (9)$$

$$\text{Range Value} = \frac{\text{Max.Vulnerability value} - \text{Min.Vulnerability value}}{3\ (\text{vulnerability class})} \quad (10)$$

The highest final vulnerability score is considered to have the greatest vulnerability and the lowest final vulnerability score is considered to have the least vulnerability.

4 RESULTS AND DISCUSSION

4.1 Ground Deformation Rate (LOS Displacement) From Satellite Image

The mapping from Line of Sight (LOS) displacement rate is shown in Figure 5. The values shown are obtained after the unwrapping process and unit conversion on the interferogram have been completed. In this case, the deformation component obtained is only the vertical component (1-dimensional deformation). A positive value indicates that the object on the earth's surface is moving toward the satellite sensor (uplift occurs), while a negative value indicates the object is moving away from the satellite sensor (subsidence). The result of the relative LOS displacement / velocity rate from satellite processing is based on the distribution of settlements. For areas where there are no settlements, the relative movement is not well mapped. From the figure it can be seen that subsidence occurred around the earthquake epicenter, with subsidence rate < -5 cm/year (Figure 5a). In contrast, around the city of Padang, uplift with a rate of > 1 cm/year occurred (Figure 5c). Several other regencies around the epicenter also experienced various uplifts and subsidence (Figure 5b).

The occurrence of landslides around the epicenter area indicates the ground movement when an earthquake occurs. Data from the Pasaman earthquake BMKG survey team showed that there were several landslide points scattered around the earthquake epicenter to some distance from the earthquake center (figure 5A, shown in blue circles). The location of the observed landslide points corresponds to the rate of subsidence around the epicenter, located at MAN 4 Timboabu, West Pasaman (figure 6). In addition to earthquakes, other factors could have triggered and contribute the landslides, such as rainfall factors, slopes, and soil types. From the Vs30 measurement around MAN 4, the soil type is moderate which is quite vulnerable when an earthquake occurs. The geological conditions around the landslide area are generally composed of Pre-Tertiary rocks in the form of metamorphic rocks, Tertiary-aged rocks in the form of sedimentary rocks and volcanic debris, and Quaternary deposits. The western part of epicenter is Quaternary deposits. Steep slopes formed by fault lines will become landslide-prone areas. Quaternary deposits and rocks of Pre-Tertiary and Tertiary age that have undergone weathering are soft, loose, unconsolidated, and strengthen the effects of shocks, making the area prone to landslides. In addition, the morphology of the hills is composed of Pre-Tertiary and Tertiary rocks that have undergone weathering, making the soil susceptible to movement.

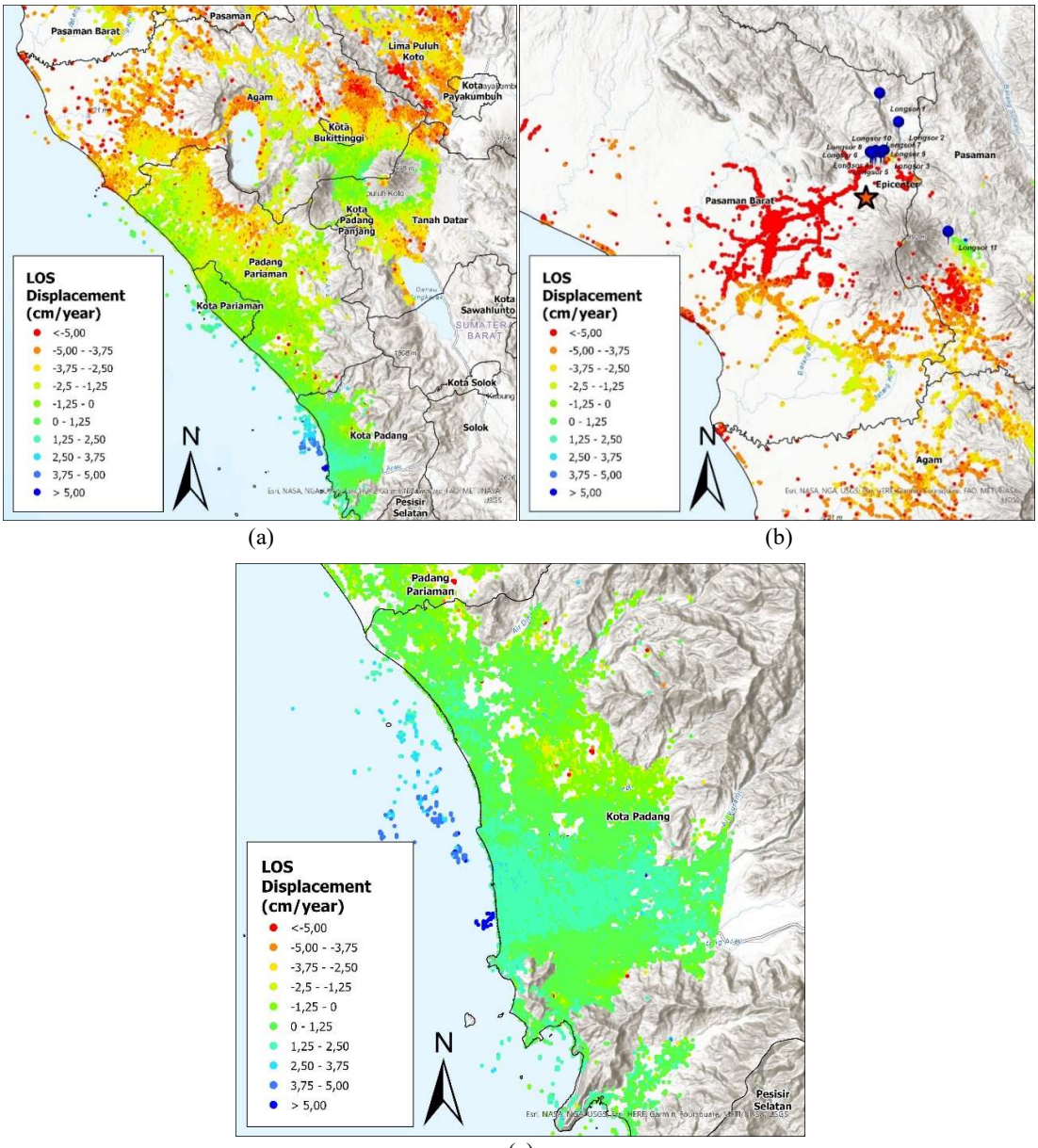

Figure 5. Deformation rate of displacement relative to the direction of view of the satellite, (a) around the epicenter, there is a decrease (subsidence), (b) several other areas are affected, and (c) around the city of Padang there is an increase (uplift).

Figure 6. Location of landslides at MAN 4 Timboabu, West Pasaman, West Sumatra

4.2 Vulnerability Identification Results

For vulnerability identification, in addition to the LOS displacement indicator discussed in previous section, the Vs30 indicator results, corrected shakemap and presence of settlement are the other 3 indicators. Results from Vs30 were previously shown in table 2. Based on the classification of Vs30 shown in Table 3b, the vulnerability score for the measured points are 4. For areas that had a significant earthquake impact, namely the Kajai area, several houses suffered severe damage and there was a mosque that collapsed, namely the Kajai Mosque. Residential areas that experienced damage have a score of 5 with a weightage of 30% (Table 3d) The landslide point area can be used as one of the validations of the subsidence in the area which can be seen in Figure 6. The scoring for the rate of soil movement in this area has a value of 4 with a weightage of 30% (Table 3a). The West Pasaman Regent's office, which is the farthest measurement location from the epicenter suffered only

minor damage The result of the rate of ground movement in this area is still dominated by subsidence. From the corrected isoseismal shakemap (figure 3) shows that the location near the epicenter of the earthquake has an intensity of VII – VIII MMI. The score for shakemap in the Pasaman region is 5 with a weightage of 20% (Table 3c). Figure 7 shows the results of vulnerability assessment for Pasaman regency.

As seen in Figure 7, there are three types of circles with different colors indicating the level of vulnerability. Areas that have a high vulnerability value generally have high rate of subsidence, more than 5 cm per year. Those areas are also a residential area, and has suffered significant damage during the Pasaman earthquake. The high vulnerable areas are also from areas with VI MMI category in the shake map. Areas that have a moderate vulnerability value generally have a rate of ground movement in the form of subsidence and uplift below 5 cm per year. The residential area in the moderate vulnerability zone suffered light damage during the Pasaman earthquake. The area with moderate vulnerability are from areas with V MMI category in the shake map. Areas that have low vulnerability values generally have a rate of ground movement in the form of subsidence and uplift ranging from -2.5 to 2.5 cm per year. The residential area in low vulnerability areas did not suffer any damage during the Pasaman earthquake. The area with low vulnerability also falls on area with < I to III MMI category in the shake map.

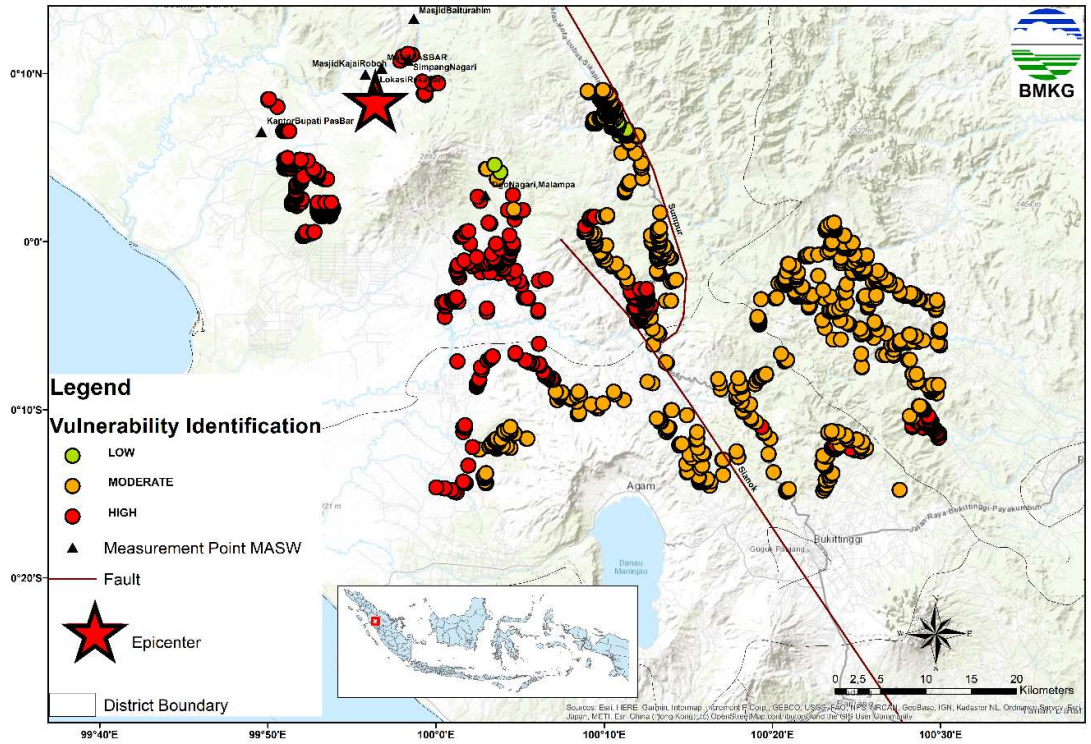

Figure 7. Vulnerability Identification Map around the epicenter due to the Pasaman earthquake on February 25, 2022.

5 CONCLUSIONS

(a) Vulnerability identification is the potential for a system or unit in experiencing problems. For Pasaman regency: in the district of Pasaman, Bonjol, Pasaman, Palembaya and Lubuk Basung, the vulnerability risk can be categorized to high, medium or low categories. It was found that areas with high vulnerability generally have a subsidence rate of more than 5 cm per year, standing on moderate soil types, as well as prone to strong shock levels. The site with high vulnerability was found to suffer significant damage due to the Pasaman earthquake. The Pasaman earthquake that occurred on 25th February is also in the same range as the shake map, i.e., VI MMI.

(b) Areas that have moderate vulnerability values generally have a movement rate in the form of subsidence and uplift of less than 5 cm per year. The areas also have medium soil type and fall in V MMI category on the shake map. The areas in moderate vulnerability suffered from light damage during the Pasaman Earthquake.
(c) Areas that have a low vulnerability value generally have a movement rate in the form of subsidence and uplift ranging from -2.5 to 2.5 cm per year. The low vulnerability area also has medium soil type but fall under < I to III MMI on the shake map. Areas categorized as low vulnerability did not suffer any damage during the Pasaman earthquake.
(d) With the vulnerability mapping, it is possible to allocate/focus provision and disaster mitigation to areas with high vulnerability, minimizing losses and impacts caused by future earthquakes.

DISCLAIMER

The author has no competing interests to declare that are relevant to the content of this article.

AVAILABILITY OF DATA AND MATERIALS

All data are available from the author.

ACKNOWLEDGMENTS

Appreciation to Seismotek BMKG for providing the opportunity to take part in training on satellite image processing and post-earthquake survey data in Pasaman on 25 February 2022. The award is also for supporting satellite image processing software licenses from ADB (Asian development bank) and the geohazard software team.

REFERENCES

Arifin, Z., 2010. *Pola Spasial Kerentanan Bencana Alam (Studi Kasus Kabupaten Cianjur)*. Tesis Magister Ilmu Geografi. Fakultas Matematika dan Ilmu Pengetahuan Alam. Universitas Indonesia.

Chen C. W., Zebker H. A., 2002. Phase unwrapping for large SAR interferograms: statistical segmentation and generalized network models. *IEEE Transactions on Geoscience and Remote Sensing*, 40(8), pp. 1709-1719. https://doi.org/10.1109/TGRS.2002.802453

Gens R, Logan T., 2003. Alaska satellite facility software tools Manual. *Fairbanks: Geophysical Institute, University of AlaskaFairbanks*.

Goldstein R. M., Werner, C. L., 1998. Radar interferogram filtering for geophysical applications. *Geophysical Research Letters*, 25(21), pp. 4035-4038. https://doi.org/10.1029/1998gl900033

Herman, D. 2015. *Geografi Bencana Alam*. Jakarta: PT Rajagrafindo Persada.

Markogiannaki, O., Karavias, A., Bafi, D., Angelou, D., Parcharidis, I., 2020. A geospatial intelligence application to support post-disaster inspections based on local exposure information and on co-seismic DInSAR results: the case of the Durres (Albania) earthquake on November 26, 2019. *Natural Hazards*, 103, pp. 3085-3100. https://doi.org/10.1007/s11069-020-04120-7

Martinez-Graña, A. M., Goy, J. L., Cimarra, C., 2015. 2D to 3D geologic map transformation using virtual globes, flight simulators, and their applications in the analysis of geodiversity in natural areas. *Environmental earth sciences*, 73(12), pp. 8023–8034.

Martínez-Graña, A. M., Goy, J. L., Zazo, C., 2016. Geomorphological appli cations for susceptibility mapping of landslides in natural parks. *Environmental Engineering & Management Journal (EEMJ)*, 15(2), pp. 1–12.

Panuntun, H., Miyazaki, S., Fukuda, Y., Orihara, Y., 2018. Probing the Poisson's ratio of a poroelastic rebound following the 2011 Mw 9.0 Tohoku earthquake. *Geophysical Journal International,* 215(3), pp. 2206-2221. https://doi.org/10.1093/gji/ggy403

Park, C. B., Miller, R. D. and Xia, J., 1999. Multi-channel analysis of surface waves. *Geophysics*, 64(3), pp. 800 – 808.

Park, C. B., Miller, R. D. & Miura, H., 2002. Optimum field parameters of an MASW survey. *Japanese Society of Exploration Geophysics Extended Abstracts*, 36.

Park, C. B., Miller, R. D., Xia, J., and Ivanov, J., 2007. Multichannel analysis of surface waves (MASW)–active and passive methods. *The Leading Edge*, 26(1): pp. 60–64. https://doi.org/10.1190/1.2431832

Park, C. B., and Carnevale, M., 2010. Optimum MASW survey–revisit after a decade of use. *In Proceedings of GeoFlorida 2010: Advances in Analysis, Modeling & Design*, pp. 1303–1312. https://doi.org/10.1061/41095(365)130

PERKA BNPB No. 02 Tahun 2012. *Tentang Pedoman Umum Pengkajian Resiko Bencana*. Jakarta: BNPB.

Rock, N. M. S., Aldiss, D. T., Aspden, J. A., Clarke, M. C. G., Djunuddin, A., Kartawa, W., Miswar, S. J., Thompson, R. & Whandoyo, R., 1983. The Geology of the Lubuk Sikaping Quadrangle (0716), Sumatra, Scale 1: 250.000. *Geological Survey of Indonesia, Directorate of Mineral Resources, Geological Research and Development Centre, Bandung*.

Sillerico, E., Marchamalo, M., Rejas, J. G., Martínez, R., 2010. La técnica DInSAR: bases y aplicación a la medición de subsidencias del terreno en la construcción. *Informes de la Construccion*, 62(519), pp. 47-53.

SNI 1726:2019., 2019. *Tata cara perencanaan ketahanan gempa untuk struktur bangunan gedung dan non gedung*. Badan Standarisasi Nasional (BSN), 2019: BSN ICS 91.120.25;91.080.01.

UNISDR, 2009., 2009. *UNISDR Terminology on Disaster Risk Reduction*. United Nations Office for Disaster Risk Reduction.

Xia, J., Miller, R. D., Park, C. B. and Ivanov, J. 2000. Construction of 2-D vertical shear-wave velocity field by the multichannel analysis of surface wave technique. *Proceedings of the Symposium on the Application of Geophysics to Engineering and Environmental Problems (SAGEEP 2000)*, pp. 1197-1206.

Xia, J. 2014. Estimation of near-surface shear-wave velocities and quality factors using multichannel analysis of surface-wave methods. *Journal of Applied Geophysics*, 103: pp. 140–151. https://doi.org/10.1016/j.jappgeo.2014.01.016

Xia, J., Miller, R. D., Park, C. B., and Tian, G. 2003. Inversion of high frequency surface waves with fundamental and higher modes. *Journal of Applied Geophysics*, 52(1), pp. 45–57. https://doi.org/10.1016/S0926-9851(02)00239-2

Xu X., Sandwell D. T., Smith-Konter, B., 2020. Coseismic Displacements and Surface Fractures from Sentinel 1 InSAR: 2019 Ridgecrest Earthquakes. *Seismological Research Letters*, 91(4), pp. 1979-1985. https://doi.org/10.1785/0220190275

Vidal Montes, R., Martínez-Graña, A. M., Martínez Catalán, J. R., Ayarza, P., Sánchez San Román F. J., 2016. Vulnerability to groundwater contamination, (SW Salamanca, Spain). *Journal of Maps*, 12, pp. 147–155.

Worden, C. B, Gerstenberger, M. C., Rhoades, D. A., and Walkd, D. J., 2012. Probabilistic Relationship Between Ground Motion parameter and Modified Mercalli Intensity in California. *Bulletin of the Seismological Society of America*, 102(1), pp. 204–221. https://doi.org/10.1785/0120110156

- This page is intentionally left blank -